Applied Surface Science 417 (2017) 54–63

Contents lists available at ScienceDirect

Applied Surface Science

journal homepage: www.elsevier.com/locate/apsusc

Full length article

Generation of nanocrystalline surface layer in short pulse laser processing of metal targets under conditions of spatial confinement by solid or liquid overlayer

Maxim V. Shugaev, Cheng-Yu Shih, Eaman T. Karim, Chengping Wu, Leonid V. Zhigilei *

Department of Materials Science and Engineering, University of Virginia, 395 McCormick Road, Charlottesville, VA 22904-4745, USA

ARTICLE INFO

Article history:
Received 3 December 2016
Received in revised form 17 January 2017
Accepted 7 February 2017
Available online 9 February 2017

Keywords:
Laser processing of metal surfaces
Surface nanocrystallization
Molecular dynamics simulations
Laser processing in liquid
Spatial confinement
Laser melting and resolidification

ABSTRACT

The effect of spatial confinement by a solid or liquid overlayer on short pulse laser-induced surface microstructure modification is investigated in a series of large-scale atomistic simulations performed for Ag targets irradiated in the regime of melting and resolidification, below the thresholds for laser spallation and ablation. For Ag targets with free surfaces, the formation of a nanocrystalline region with random crystallographic grain orientation is observed under irradiation conditions leading to the generation of numerous sub-surface voids that slow down the solidification process. When no voids are generated, the resolidification produces grains misoriented with respect to the bulk of the target by just several degrees and separated from each other by low angle grain boundaries or dislocation walls. The presence of a liquid or solid overlayer suppresses nucleation of sub-surface voids, provides an additional pathway for cooling through the heat conduction to the overlayer, and facilitates the formation of nanocrystalline structure in a region of the metal target adjacent to the overlayer. Moreover, the stabilizing effect of the solid overlayer may result in an incomplete melting of metal in the vicinity of the interface, making it possible for grains growing from the interface to retain "memory" of the target orientation and to produce nanocrystalline interfacial region with small misorientation of grains with respect to the bulk of the target. In all simulations, the nanocrystalline layers generated by laser processing of single crystal Ag targets are characterized by a high density of stacking faults, twin boundaries, and point defects produced in the course of the rapid resolidification.

1. Introduction

Laser processing of metal surfaces in liquid environment and in the presence of a solid overlayer has a number of distinct characteristics that may be beneficial for practical applications. The confining effect of optically transparent solid or liquid layers covering irradiated targets can alter the dynamics of material decomposition and ejection in the ablation regime [1–5], thus directly affecting the surface morphology of laser-modified targets. Moreover, the interaction of melted metal with an overlayer can contribute to cooling of the molten layer, thus creating conditions for stronger, as compared to laser processing in air or vacuum, undercooling and formation of highly nonequilibrium surface microstructure. Indeed, a number of experimental studies have demonstrated that the presence of liquid environment [6–14] or a solid overlayer [15–17] can have major impact on the morphology of laser-processed surfaces. The effect of the spatial confinement on the microstructure of the irradiated targets has also been demonstrated in laser shock peening experiments performed in the ablation regime [18–20].

More "gentle" microstructure modification at lower laser fluences, in the regime of melting and resolidification, however, has not been investigated in the presence of liquid or solid overlayers so far. For irradiation in vacuum or in air, the utility of short laser pulses for selective nanoscale engineering of surface microstructure has been demonstrated for various material systems. In particular, the formation of nanoscale twinned domains has recently been observed in femtosecond laser processing of Ni and explained by the onset of growth twinning under conditions of strong undercooling realized in the course of the rapid resolidification of a transiently melted surface region [21]. Even stronger undercooling of the melted region, sufficient to trigger massive nucleation of new crystallites and generation of nanocrys-

* Corresponding author.
E-mail address: lz2n@virginia.edu (L.V. Zhigilei).

http://dx.doi.org/10.1016/j.apsusc.2017.02.030
0169-4332/

talline surface layer with high density of twin boundaries and stacking faults present in the nanograins, has been predicted in recent atomistic simulations of laser processing of Ag targets [22]. The possibility of the generation of thin nanocrystalline layers with high density of twins is highly attractive, as such layers can exhibit an unusual combination of high strength and ductility [23–26], as well as enhanced catalytic activity [27,28] and tunable surface reflectance spectra [29]. The results of the simulations, however, suggest that the laser-induced generation of nanocrystalline layer on the surface of a pure Ag target is only possible in a narrow range of laser fluences close to the spallation threshold, when the generation sub-surface voids slows down the propagation of the resolidification front from the bulk of the target [22]. This leads to an intriguing question on whether the presence of liquid or solid overlayer could broaden the range of irradiation conditions that yield surface nanocrystallization and result in the formation of a nanocrystalline surface layer without the generation of sub-surface voids.

In this paper, we investigate the specific mechanisms of overlayer-assisted surface nanostructuring by performing a series of large-scale atomistic simulations of short pulse laser irradiation of Ag targets in water environment and under confinement by a silica glass overlayer, and contrasting the results of these simulations to the ones obtained for similar irradiation conditions in vacuum. The main focus of the analysis of the simulation results is on revealing the irradiation conditions and mechanisms responsible for the generation of nanocrystalline surface layer and establishing the processes that control the structural characteristics of the nanocrystalline layer. A brief description of the computational model is provided below, in Section 2, and is followed by presentation of the simulation results in Section 3 and summary in Section 4.

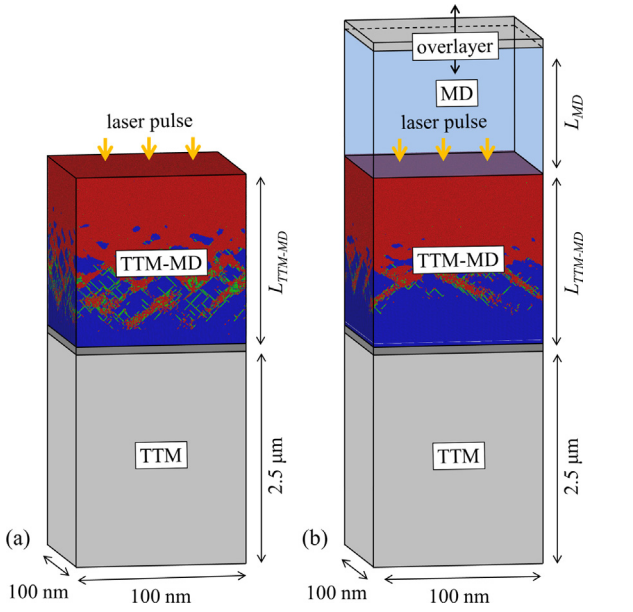

Fig. 1. Schematic sketches of the computational setups used in MD simulations of laser interaction with metal targets in vacuum (a) and in the presence of an optically transparent solid or liquid overlayer (b). The top part of the target is represented by TTM-MD model, whereas the temperature evolution in the deeper part is described by TTM equations. Molecular dynamics representation is used for parts of the solid or liquid overlayers adjacent to the target, as shown by the blue rectangular parallelepiped in (b). At the bottom of the TTM-MD and on the top of the MD regions the pressure wave transmitting boundary conditions are imposed. The boundary conditions mimic the non-reflective propagation of laser-induced pressure waves in the Ag target and the overlayer, which are assumed to be sufficiently thick to ensure that any effects caused by the reflection of the waves from the outer surfaces of the target and overlayer can be neglected. Periodic boundary conditions are applied in the lateral directions, parallel to the surface of the target. (For interpretation of the references to colour in this figure legend, the reader is referred to the web version of this article.)

2. Computational model

The computational setups used in the simulations of laser interactions with bulk Ag targets in vacuum and in the presence of liquid or solid overlayer are schematically illustrated in Fig. 1. In all simulations, the top part of the Ag target is simulated with a hybrid atomistic–continuum model [30] that combines the classical molecular dynamics (MD) method [31] with the continuum-level two-temperature model (TTM) [32]. The model accounts for the laser excitation of conduction-band electrons, electron-phonon coupling, and the fast electron heat conduction from the hot surface region of the irradiated target to the bulk of the target. At the same time, the atomistic representation of the surface region of the target enables detailed analysis of the kinetics and mechanisms of laser-induced structural and phase transformations. The electronic heat transfer in the deeper part of the target, where no structural changes take place in response to the laser irradiation, is described by the conventional TTM. The depth covered by the TTM is chosen to be 2.5 μm to ensure a negligible temperature change at the bottom of the computational system by the end of the simulation. The absorption of laser energy is represented through a source term added to the TTM equation for the electron temperature [30]. The source term has a temporal Gaussian profile and includes a description of the ballistic energy redistribution by the excited electrons through an appropriate modification of the effective energy deposition depth [30,33]. The optical absorption depth, 12 nm at laser wavelength of 800 nm [34], and the effective depth of the ballistic energy transport, estimated to be about 56 nm for Ag [22,35] are used in the simulations reported in this paper.

A dynamic pressure wave transmitting boundary condition [36,37] is applied at the bottom of the TTM-MD part of the model to ensure nonreflecting propagation of the laser-induced stress wave into the bulk of the target. Periodic boundary conditions are applied in the lateral directions, parallel to the irradiated (001) surfaces of the Ag targets, and the dimensions of the computational systems in these directions are about 100 nm × 100 nm. The interatomic interactions are described by the embedded atom method (EAM) potential parametrized for Ag [38]. Before applying laser irradiation, all computational systems are thermalized at 300 K for 150 ps. A complete description of the combined atomistic-continuum model is provided elsewhere [22,30], and all the parameters of the model for simulation of laser interaction with a Ag target are given in Ref. [22]. Thus, below we only delineate parameters of the computational setups specific for the simulations reported in this paper and provide a brief description of the model representations of the liquid and solid overlayers.

Since the goal of this study is to explore the possibility of laser-induced surface nanocrystallization, the irradiation conditions in all simulations are chosen to produce transient melting and resolidification of a surface region of the target. The simulations of laser interaction with Ag targets in vacuum are performed for two sets of irradiation parameters (laser pulse duration τ_p and absorbed laser fluence F_{abs}). The first set, $\tau_p = 100$ fs and $F_{abs} = 850$ J/m^2, corresponds to the formation of a porous sub-surface region covered by a nanocrystalline surface layer, as discussed in detail in Ref. [22]. The second set is performed with $\tau_p = 10$ ps and $F_{abs} = 900$ J/m^2 and results in the melting and resolidification of ~60 nm surface layer without nucleation of sub-surface voids. The depth of the surface part of the Ag target represented with atomistic resolution, L_{TTM-MD} in Fig. 1, is 150 nm for the first set and 103 nm for the second set of irradiation parameters, which corresponds to 84.2 and 62.5 million

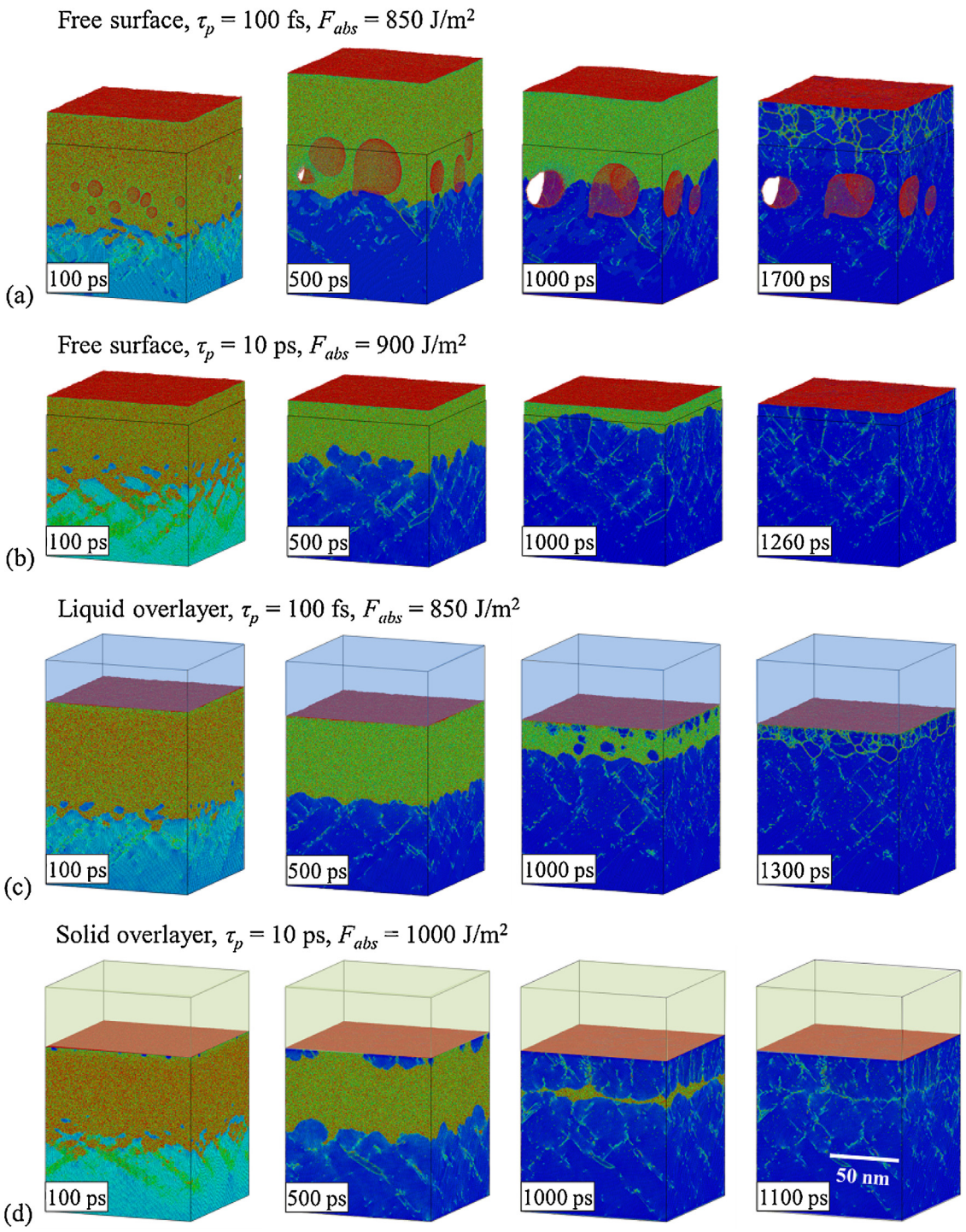

Fig. 2. Snapshots of atomic configurations generated in TTM-MD simulations of laser irradiation of Ag targets in vacuum (a, b), in water environment (c), and in the presence of a solid silica overlayer (d). The laser pulse durations τ_p and absorbed laser fluences F_{abs} are indicated on the corresponding panels. Only the regions that correspond to the top 100 nm parts of the targets before the irradiation are shown in the snapshots. The boxes in (a) and (b) outline the initial position of the target before the irradiation, while boxes in (c) and (d) also include parts of the overlayers extending up to 50 nm from the original surface. The atoms are colored by their potential energies, with the scale from −2.84 eV (blue) to −2.64 eV (red) chosen to ensure that the crystalline parts of the targets are blue, the melted regions are green, and the free surfaces are red. Crystal defects, such as vacancies, dislocations, stacking faults, and grain boundaries, can also be distinguished as regions with elevated potential energy. To reduce thermal noise in potential energies, the atomic configurations are quenched for 1–2 ps using the velocity-dampening technique. (For interpretation of the references to colour in this figure legend, the reader is referred to the web version of this article.)

Ag atoms, respectively (the lateral size of the computational cell used in the second simulation is slightly larger, 103 nm × 103 nm).

The simulation of laser melting and resolidification in liquid environment is performed for irradiation parameters of τ_p = 100 fs and F_{abs} = 850 J/m². These parameters are the same as in the first simulation in vacuum, making it possible to directly compare the results and elucidate the effect of the liquid environment on the material response to the laser excitation. The TTM-MD part of the model has a depth of L_{TTM-MD} = 200 nm and consist of about 114.8 million Ag atoms. The liquid environment above the

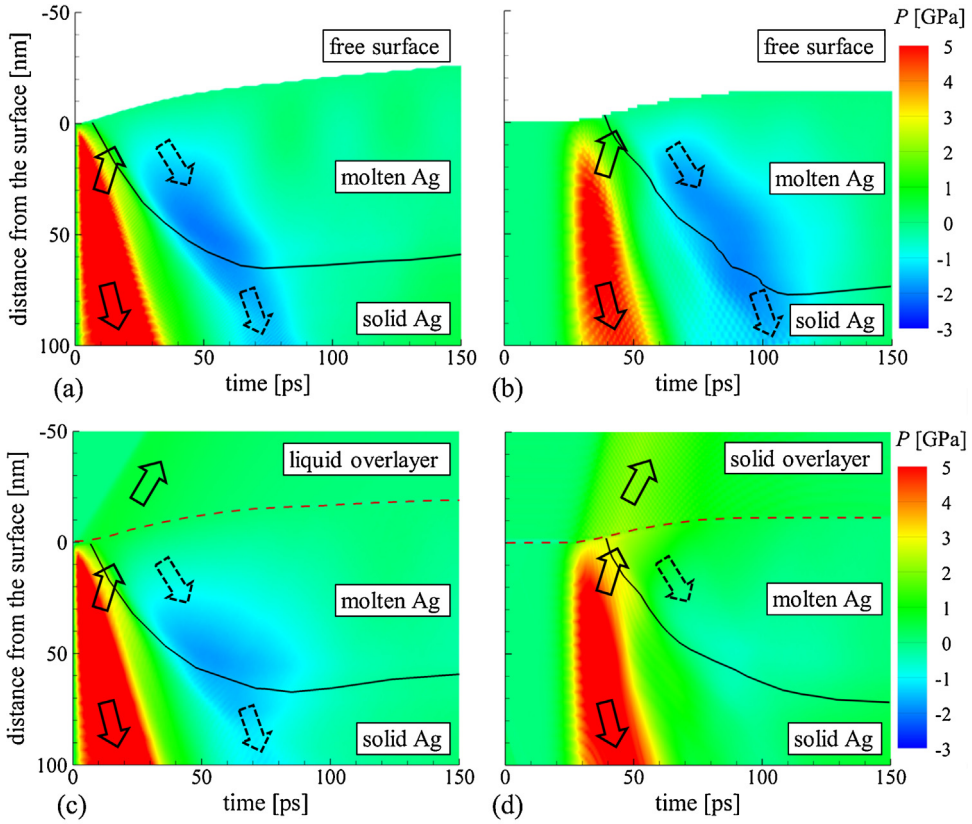

Fig. 3. Contour plots of the spatial and time evolution of pressure in TTM-MD simulations of laser irradiation of Ag targets in vacuum (a, b), in water environment (c), and in the presence of a solid silica overlayer (d). The targets are irradiated by 100 fs laser pulses at 850 J/m^2 in (a) and (c), by a 10 ps pulse at 900 J/m^2 in (b), and by a 10 ps pulse at 1000 J/m^2 in (d). The laser pulse is directed along the vertical axis from the top of the contour plots. The solid black curves separate melted and solid parts of the Ag targets. The dashed red curves in (c, d) show the position of the Ag-overlayer interface. The arrows schematically show the directions of the propagation of laser-induced pressure waves. The compressive waves, shown by the solid arrows, are generated by the fast laser heating of the surface regions of the targets and can partially propagate into the overlayers in (c) and (d), thus decreasing the amplitude of the unloading tensile waves shown by dashed arrows. In (b) and (d), the maximum intensity of the 10 ps laser pulse is reached at 25 ps. The snapshots from the simulations are shown in Fig. 2. (For interpretation of the references to colour in this figure legend, the reader is referred to the web version of this article.)

Ag target is described by a combination of a coarse-grained MD model parametrized for water [5,39,40] and a dynamic acoustic impedance matching boundary condition [35]. The coarse-grained MD model represents several water molecules by a single particle, which drastically increases the computational efficiency of the model. Despite the reduced, as compared to real water, number of dynamic degrees of freedom, the coarse-grained MD model enhanced by an advanced local heat bath approach [5,39,40] is capable of reproducing, at a semi-quantitative level, many of the relevant experimental properties of real water. In particular, the density and heat capacity are directly fitted to the experimental values, while the speed of sound, bulk modulus, viscosity, surface energy, melting temperature, critical temperature, and critical density do not deviate from the experimental values by more than 25% [5]. The thickness of a part of water overlayer represented by the coarse-grained MD model is L_{MD} = 300 nm, and the corresponding number of coarse-grained particles is 36.1 million. The dynamic impedance matching boundary condition based on an imaginary plane approach [35] is applied at the top of the coarse-grained MD region to ensure nonreflecting propagation of the pressure wave generated at the metal-water interface into the bulk of the water environment. This boundary condition mimics the response of an infinitely thick overlayer and is suitable for simulation of experimental conditions, where the reflection of the pressure wave from the outer surface of the water overlayer does not have any significant effect on processes occurring in the vicinity of the irradiated metal surface.

The effect of the solid transparent overlayer on the microstructure modification is studied for irradiation parameters of τ_p = 10 ps and F_{abs} = 1000 J/m^2. These irradiation conditions result in approximately the same melting depth as in the second simulation performed in vacuum, where the same pulse duration but a lower laser fluence of 900 J/m^2 is used. The overlayer is represented by MD model with particles interacting with each other through Lennard-Jones potential fitted to approximately reproduce the elastic properties and melting temperature of fused silica glass. Similar to the liquid overlayer, the dynamic impedance matching boundary condition is applied at the top of the MD region to simulate nonreflecting propagation of the laser-induced pressure wave into the bulk part of a thick overlayer. Details of the implementation and parametrization of the computational description of the silica overlayer are providers in Ref. [35]. The initial sizes of the TTM-MD and MD computational domains are L_{TTM-MD} = 103 nm and L_{MD} = 103 nm, which corresponds to 62.5 million Ag atoms and 13.5 million "silica" particles, respectively.

3. Simulation results

The effect of the liquid and solid overlayers on the ability of short pulse laser irradiation of metal targets to produce nanocrystalline surface layers is investigated by comparing results of the simulations performed in vacuum and in the presence of the overlayers. Computational predictions for irradiation in vacuum are described

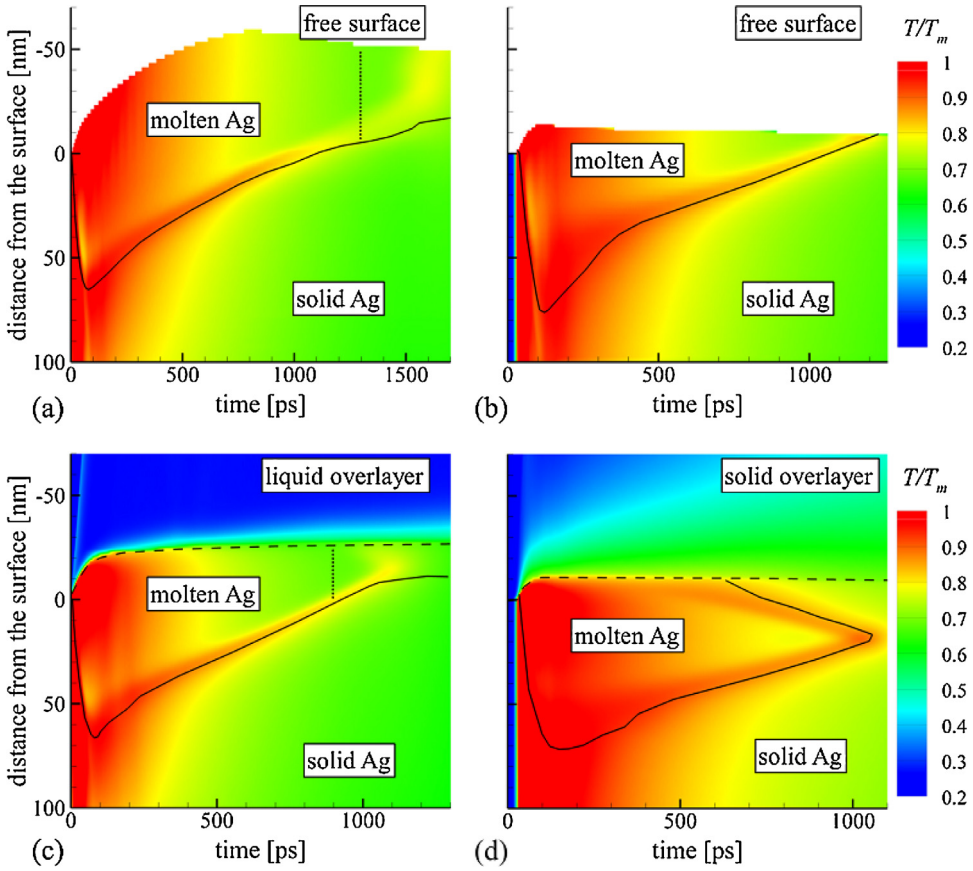

Fig. 4. Contour plots of the long-term spatial and time evolution of temperature in TTM-MD simulations of laser irradiation of Ag targets in vacuum (a, b), in water environment (c), and in the presence of a solid silica overlayer (d). The targets are irradiated by 100 fs laser pulses at 850 J/m^2 in (a) and (c), by a 10 ps pulse at 900 J/m^2 in (b), and by a 10 ps pulse at 1000 J/m^2 in (d). The laser pulse is directed along the vertical axis from the top of the contour plots. The temperature scale is normalized by the melting temperature of EAM Ag, T_m. The maximum temperature reached in the Ag target is 1.60 T_m in (a), 1.33 T_m in (b), 1.63 T_m in (c) and 1.49 T_m in (d). The solid curves separate melted and solid parts of the Ag targets. The dashed curves in (c, d) show the position of the Ag-overlayer interface. The vertical dotted lines in (a) and (c) mark the times when the nucleation of the first crystallites is detected in the undercooled surface regions of the Ag targets. The snapshots from the simulations are shown in Fig. 2. (For interpretation of the references to colour in this figure legend, the reader is referred to the web version of this article.)

first and are followed by the results for laser processing in liquid environment and in the presence of a solid overlayer.

3.1. Generation of nanocrystalline surface layer by laser irradiation in vacuum

The first simulation of laser-induced melting and resolidification of Ag target in vacuum, performed at τ_p = 100 fs and F_{abs} = 850 J/m^2, has already been described in Ref. [22], and only a brief summary of the results is provided here. The snapshots from the simulation are shown in Fig. 2a, where the atoms are colored by their potential energy, so that the melted and solid parts of the target can be easily distinguished. Laser excitation of the conduction band electrons followed by the rapid energy transfer from the hot electrons to the lattice through electron-phonon coupling leads to the superheating and melting of an about 70-nm-deep surface region of the target within the first tens of picoseconds after the laser pulse. Due to the fast heat conduction to the bulk of the target, the temperature of the liquid-solid interface drops below the equilibrium melting temperature of the EAM Ag material, T_m = 1139 K, and the melting gives way to resolidification by ~75 ps.

The melting and resolidification are occurring simultaneously with the generation and dynamic relaxation of laser-induced stresses that are illustrated in Fig. 3a. The rapid temperature increase in the surface region of the target takes place under conditions of stress confinement [41–44] and results in a build-up of strong compressive stresses, as can be seen from Fig. 3a. The relaxation of the compressive stresses in the presence of the free surface of the target results in the generation of an unloading tensile wave marked by dashed arrows in Fig. 3a. The tensile stresses, shown by blue color in Fig. 3, are sufficiently strong to induce cavitation in the lower part of the melted region, with the appearance of small cavities already apparent in the snapshot shown for 100 ps in Fig. 2a. The cavities grow, coalesce, and are eventually trapped by the solidification front advancing from the crystalline part of the target. The movement of the front of the epitaxial solidification can be followed in Fig. 4a, where the location of the front is shown by a black line. The presence of voids impedes the solidification front propagation, extends the time that the top surface layer of the target remains in the molten state, and contributes to the generation of increasingly deep undercooling in the melted surface region. At about 1300 ps, when the surface temperature drops down to ~0.69 T_m, a massive nucleation of small crystallites is initiated throughout the deeply undercooled liquid region and results in the formation, within the next 400 ps, of a nanocrystalline layer with ultrafine grains featuring random crystallographic orientation and a high density of stacking faults and twin boundaries [22]. Similar to the solidification front propagation, the homogeneous nucleation of new crystallites leads to the release of the latent heat of melting and is reflected in a noticeable temperature increase in the surface region of the target, Fig. 4a.

The observation of the formation of the nanocrystalline layer covering the porous subsurface region leads to a question on whether it is possible to induce surface nanocrystallization of the

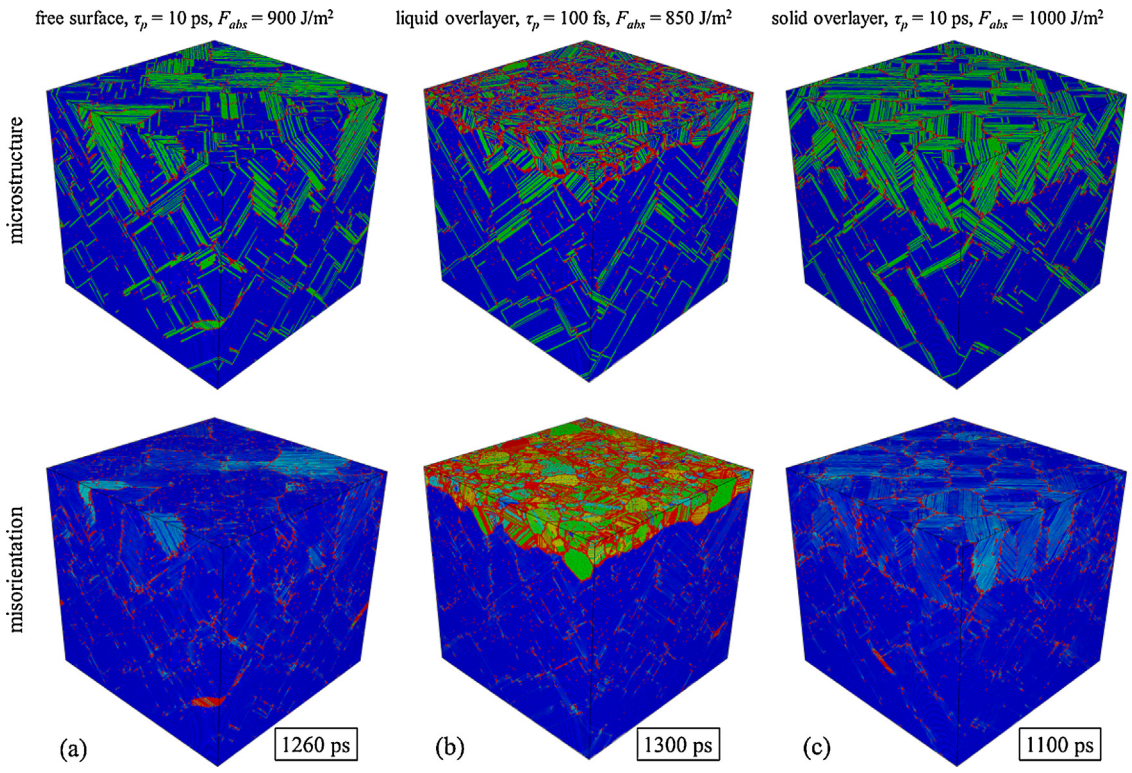

Fig. 5. Snapshots of atomic configurations generated at the end of resolidification process in TTM-MD simulations of laser irradiation of Ag targets in vacuum (a), in water environment (b), and in the presence of a solid silica overlayer (c). The laser pulse durations τ_p and absorbed laser fluences F_{abs} are indicated on the corresponding panels. The top 1 nm layers of the targets are blanked to expose the underlying defect structures. *In the upper panels*, the atoms are colored by their local structural environment, so that the fcc and hcp atoms are blue and green, respectively, and the red atoms have unidentified local crystal structure. With this coloring scheme, the single and double green layers on a blue background correspond to twin boundaries and stacking faults in the fcc structure, respectively. Unidentified atoms belong to grain boundaries, dislocation cores, and point defects. *In the lower panels*, the atoms are colored by the smallest angle between one of the ⟨111⟩ directions of the original fcc lattice and a ⟨111⟩ direction in the corresponding grain. The blue to red color scale corresponds to misorientation angles ranging from 0° to 30°. (For interpretation of the references to colour in this figure legend, the reader is referred to the web version of this article.)

Ag target without the generation of sub-surface voids. To address this question, another simulation is performed with τ_p = 10 ps and F_{abs} = 900 J/m². The absorbed fluence of 900 J/m² is above the spallation threshold for τ_p = 100 fs, as has been demonstrated in Ref. [45], where the separation and ejected of a molten layer is observed. The use of a longer 10 ps laser pulse, however, allows for a partial relaxation of thermoelastic stresses during the laser-induced heating and prevents the generation of voids. As can be seen from the snapshots shown in Fig. 2b and the solidification curve shown in Fig. 4b, the epitaxial solidification front proceeds all the way to the surface, and no nucleation of new crystallites is observed in the surface region. In the absence of voids impeding the propagation of the solidification front, the front reaches the surface faster, before the critical undercooling of 0.69 T_m required for the onset of massive homogeneous crystallization is achieved in the melted part of the target.

Despite the absence of the nucleation of new crystallites, the microstructure of the resolidified surface region features a high density of the stacking faults and twin boundaries, which can be attributed to the highly nonequilibrium conditions of the rapid solidification, as well as the small energy of these defects in the EAM Ag material [46]. Moreover, several distinct surface domains misoriented with respect to each other by several degrees and separated by low-angle grain boundaries (dislocation walls) are also identified in the surface region, Fig. 5a. The formation of these domains can be explained by the rough morphology of the liquid-crystal interface formed by the end of the rapid melting process. The melting proceeds on the same timescale the unloading wave develops and propagates through the melting front, leading to the emission of numerous partial dislocations from the melting front. The stacking faults left behind by the partial dislocations can be seen as green stripes appearing below the melting region in Fig. 6a. The dislocation emission into the superheated part of the crystal facilitates nucleation of liquid regions at the defect sites and produces a mixed molten-crystalline structure at the melting front. Some of the crystalline regions in this mixed region are fully or partially surrounded by liquid and may undergo small stochastic rotations prior to merging into the continuous solidification front that can be seen at a later time in Fig. 2b. The growth of the crystallites that are tilted with respect to the original crystallographic orientation of the target is responsible for the generation of the slightly misoriented domains/grains in the surface region of the target, Fig. 5a.

3.2. *Effect of liquid environment on surface nanocrystallization*

The results of the simulations performed for targets with free surfaces suggest that it is difficult to expect generation of a nanocrystalline surface layer on a (001) Ag target without the concurrent formation of a sub-surface porous region that corresponds to an incomplete spallation conditions. This leads to the question on the possibility of using a liquid or solid overlayer that could suppress the generation of sub-surface voids, contribute to the cooling of the metal target, and facilitate the surface nanocrystallization. This possibility is explored in this section for a liquid overlayer parametrized for water as described in Section 2.

The large-scale simulation of laser interaction with a Ag target in liquid environment is performed with the same irradiation condi-

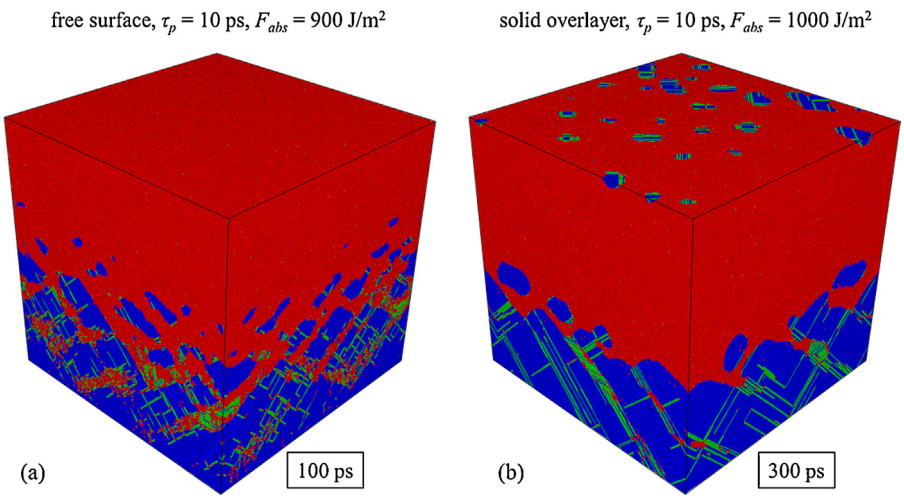

Fig. 6. The snapshot of atomic configurations of Ag target with free surface (a) and covered by a silica glass overlayer (b) taken at 100 and 300 ps after laser irradiation. The laser pulse durations τ_p and absorbed laser fluences F_{abs} are indicated on the corresponding panels. The coloring scheme is the same as in upper panels of Fig. 5, but the red color is also used for molten Ag. The snapshots illustrate the presence of crystalline regions surrounded by liquid within the melting front in (a) and crystalline regions stabilized by the overlayer in (b). Animated sequences of snapshots from these simulations with a time resolution of 100 ps can be found in the Supplementary Material for this article and on this web site [47]. (For interpretation of the references to colour in this figure legend, the reader is referred to the web version of this article.)

tions as the first simulation in vacuum discussed above, where the generation of a nanocrystalline layer covering a porous sub-surface layer (Fig. 2a) is observed. The snapshots from the simulation are presented in Fig. 2c, while the pressure and temperature contour plots are shown in Figs. 3 c and 4 c, respectively. Two notable effects, apparent from the visual inspection of the snapshots, are (1) the absence of the sub-surface voids in the molten part of the target and (2) the onset of the nucleation of new crystallites near the surface of the target at the final stage of the solidification process. These two effects are discussed next.

The absence of the sub-surface voids can be explained based on the evolution of the laser-induced pressure illustrated in Fig. 3c. The generation of the initial compressive pressure is defined by the electron-phonon equilibration and rapid heating of the surface region occurring under conditions of the thermal and stress confinement [41–44], and is largely unaffected by the presence of the liquid environment. This is reflected in almost identical compressive parts of the pressure contour plots in Fig. 3a and c. The formation of the unloading tensile component of the pressure wave, however, is significantly affected by the liquid environment. Since the acoustic impedance of water is much lower than that of Ag, the relaxation of the compressive pressure results in the generation of both a compressive wave emitted into the water and a weaker, as compared to the simulation with free surface (Fig. 3a), tensile wave propagating into the bulk of the Ag target, as schematically shown by solid and dashed arrows in Fig. 3c. The reduced amplitude of the unloading tensile wave is not sufficient for the initiation of cavitation, which explains the absence of voids in the melted part of the target in Fig. 2c. Note that the suppression of the nucleation of subsurface voids has also been observed in earlier MD simulations of short pulse laser interactions with Ag targets performed under stronger spatial confinement by a solid silica overlayer [35], while the reduction in the number of spalled layers was reported in hydrodynamic modeling of laser ablation of Al in water [4].

The suppression of the void nucleation has important consequences for the kinetics of resolidification of the melted region. While the melting time and the maximum melting depth are very similar in the simulations performed in vacuum and in water environment, as can be seen from the similarity of the black curves showing the location of the liquid-crystal interface in Figs. 3a,c, the same black curves shown for a longer time in Fig. 4a,c clearly demonstrate the diverging resolidification behavior. The appearance of sub-surface voids not only increases the effective path the solidification front has to cover before it reaches the surface but also decreases the velocity of solidification front [22] when it passes through the region with voids. In the simulation with water overlayer, Fig. 4c, after the initial rapid apparent advancement due to the solidification of a liquid-crystalline mixture formed by the end of the melting process (similar to those shown in Fig. 6), the velocity of the resolidification front reaches a steady level of ~63 m/s. In contrast, in the simulation with free surface, Fig. 4a, the velocity of the solidification front drops below 45 m/s when the front passes through the region with voids.

The slowdown of the epitaxial solidification front by the sub-surface voids extends the time that the top surface layer of the target remains in the molten state and allows it to reach a deeper undercooling. On the other hand, the reduced effective thermal conductivity of the porous sub-surface region slows down the cooling of the top layer. As a result, it takes about 1.3 ns for the top molten layer to cool down to 0.69 T_m, when a massive homogeneous nucleation of new crystalline Ag grains is observed, Fig. 4a. In the presence of liquid environment, the surface cooling and the solidification front propagation proceed without the impediment from the voids, and the rapid nanocrystallization is initiated much earlier, at ~900 ps, Fig. 4c. The nucleation and fast growth of multiple crystallites in the undercooled liquid region result in the formation of an about 18-nm-thick nanocrystalline surface layer with grains randomly oriented with respect to the crystallographic orientation of the Ag target. Similar to the targets with free surfaces discussed in Section 3.1, the rapid solidification under conditions of strong undercooling produces complex internal structure of individual grains characterized by a high density of stacking faults and twin boundaries, Fig. 5b.

In addition to the thermal conduction to the bulk of the Ag target, the interaction with water provides an additional pathway for cooling of the Ag surface region. The efficiency of this channel is limited by the rapid superheating of water adjacent to the hot surface of the metal target and the formation of a low-density supercritical water layer with poor thermal conductivity. As a result, the total amount of the thermal energy transferred to the water overlayer by the end of the simulation is only ~2% of the energy deposited by the laser pulse. Nevertheless, this channel of cooling of the metal surface may play an important role defining the microstructure of

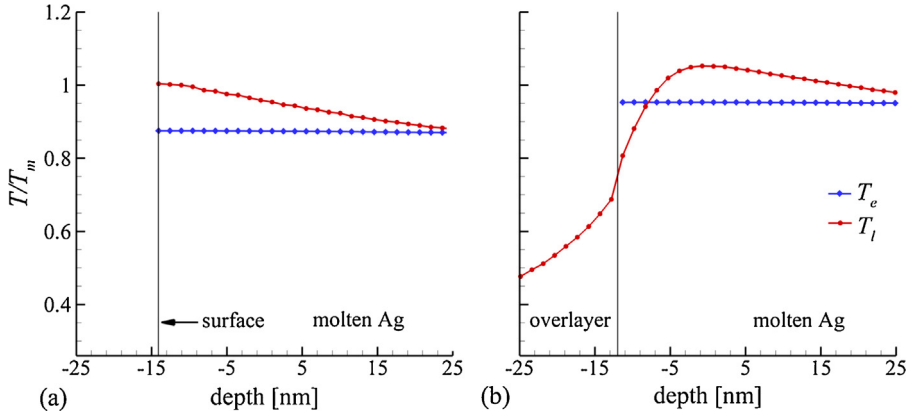

Fig. 7. The temperature distributions with depth at 100 ps after irradiation of a Ag target with free surface (a) and surface covered by a silica overlayer (b). The lattice and electron temperatures are shown by red lines/circles and blue lines/diamonds, respectively. The targets are irradiated by 10 ps pulses at absorbed fluences of 900 J/m^2 in (a) and 1000 J/m^2 in (b). The sharp drop in temperature of the molten Ag near the interface in (b) demonstrates the effect of the heat diffusion into the overlayer. (For interpretation of the references to colour in this figure legend, the reader is referred to the web version of this article.)

resolidified surface, as discussed for the case of solid overlayer in the next section.

3.3. Effect of a solid overlayer on surface nanocrystallization

The characteristic features of laser-induced modification of surface microstructure under conditions of spatial confinement by a solid transparent overlayer have both similarities to and clear distinctions from the processing in a liquid environment discussed above. Similar to liquids, the presence of a solid overlayer can suppress the generation of tensile waves and contribute to the cooling of the transiently melted region of the metal target. Both of these effects can be stronger with a solid overlayer. The acoustic impedance (product of material density and speed of sound) of the overlayer can be much closer to the one of the metal target (*e.g.*, it is only about twice lower for silica glass as compared to Ag), leading to an effective propagation of the compressive pressure wave into the overlayer and a weaker unloading wave generated in the metal target [17,35]. The higher thermodynamic stability of solid overlayers can be expected to keep the heat transfer from a hot metal surface to an overlayer uninterrupted by the formation of a layer of low-density vapor or supercritical fluid observed at the metal-liquid interface.

Moreover, in contrast to a free surface or a surface covered by a liquid, which typically do not allow for heterogeneous nucleation of new crystallites, the interface between molten metal and overlayer can facilitate the heterogeneous nucleation if the condition of $\gamma_{so} < \gamma_{lo} + \gamma_{sl}$ is satisfied (γ_{so}, γ_{lo}, γ_{sl} are the interface free energies for solid metal – overlayer, liquid metal – overlayer, and liquid metal – solid metal interfaces, respectively). Depending on the interface free energies, an overlayer may even facilitate preferable nucleation and stabilization of metastable solid phases, as exemplified by the generation of a layer of metastable bcc Cu in MD simulations of laser melting and resolidification of Cu-Ag interface [48]. Moreover, an additional cooling due the heat transfer to the overlayer combined with the stabilizing effect of the low interfacial energy may result in an incomplete melting near the interface and regrowth of the melted part of the target from both the crystalline bulk and the crystalline metal layer or islands "survived" on the overlayer. The latter effect is observed in the simulation discussed below.

The effect of a solid overlayer on the microstructure modification is illustrated by a simulation performed with $\tau_p = 10$ ps and $F_{abs} = 1000$ J/m^2. These irradiation conditions are chosen to ensure that the maximum melting depth in this simulation is similar to the one in the second simulation with free surface discussed in Section 3.1, where a lower absorbed fluence of 900 J/m^2 is used. The need for the higher fluence was defined by the inhibiting effect the overlayer has on the melting process [35]. For a target with free surface, the tensile stresses associated with the unloading wave reduce the crystal stability against melting [49] and assist in the propagation of the melting front at the final stage of the melting process, Fig. 3b. The unloading wave is significantly reduced in the presence of the overlayer, Fig. 3d, and the maximum melting depth is approximately the same in the two simulations. Despite the similarity of the melting curves in Figs. 3b and 3d, the solidification process proceeds very differently in the two simulations. In the case of the free surface, a single solidification front propagates from the solid part of the target and sweeps the entire melted region, as can be seen from Figs. 2 b and 4 b. In the simulation with the solid overlayer, however, the solidification also proceeds from several areas adjacent to the overlayer, and the growing crystalline islands merge into the second solidification front that meets the one advancing from the bulk of the target at a depth of about 25 nm below the interface, Figs. 2 d and 4 d.

The reason for the appearance of the second solidification front in this simulation is apparent from the inspection of a snapshot of an atomic configuration shown in Fig. 6b for a time of 300 ps. The stabilizing effect of the overlayer makes it possible for several small islands of the original crystal to survive the thermal spike induced by the laser irradiation. These islands start growing immediately after the temperature of the molten Ag drops below T_m, without the need for any undercooling. As illustrated in Fig. 5c, the final microstructure of the resolidified layer consists of nanograins with sizes in the range of 20–30 nm. The nanograins are slightly misoriented with respect to each other and the bulk of the target. The interfacial islands from which the nanograins grow largely retain the "memory" of the original crystallographic orientation of the target and, similarly to the crystalline islands generated at the melting front (Fig. 6a), are slightly misoriented due to the random statistical fluctuations during the melting and resolidification process.

The temperature distributions shown in Fig. 7 for a time of 100 ps further illustrate the reason for the survival of the crystalline islands near the overlayer. While cooling due to the heat transfer to the cold overlayer only affects an about 10-nm-thick layer of the metal target, Fig. 7b, it is sufficient to prevent the complete melting of the layer. In the absence of the overlayer, Fig. 7a, the temperature of the surface is the highest at the surface, as expected. The electron temperature shown in Fig. 7 by blue lines deviates from the vibrational temperature (also called "lattice" temperature in TTM) due to the relatively weak electron-phonon coupling in Ag [50]. The high electron thermal conductivity of Ag prevents the appear-

ance of any sharp electron temperature gradients and keeps the electron temperature profiles flat. The depth of the temperature drop in the surface region of the metal target affected by the vibrational/phononic thermal conduction to the overlayer is, therefore, defined not so much by the electronic thermal conductivity of the metal, but by the strength of the electron-phonon coupling that controls the degree of the electron-phonon nonequilibrium in the interfacial region. A similar effect of splitting between the electron and vibrational temperatures has earlier been found to play an important role in defining the kinetics of rapid melting [51] and solidification [52] in metals.

Finally, we would like to note that, although the temperature of the melted Ag stayed above the critical undercooling of $0.69\,T_m$ required for the onset of massive homogeneous nucleation of new crystallites during the resolidification process, this does not mean that the homogeneous nucleation is not possible in short pulse laser processing of metal targets covered by a solid overlayer. On the contrary, when slightly higher laser fluence is applied in smaller-scale simulations performed with the solid overlayer, the top part of the target is completely melted, the second solidification front is not created, and the region of the target adjacent to the overlayer is readily undercooled down to the temperature required for the rapid homogeneous nucleation of new crystallites. Moreover, the cooling due to the heat conduction to the overlayer and the reduced free energy barrier for heterogeneous nucleation of new crystallites at the metal-overlayer interface are the factors facilitating the nanocrystallization in the presence of the overlayer. The final microstructure in this case is expected to be similar to that observed in the simulation with a water overlayer, Fig. 5b, *i.e.*, instead of slightly misoriented grains, a layer of randomly oriented grains is likely to be formed.

4. Summary

The mechanisms responsible for modification of surface microstructure in short pulse laser processing of metal targets in vacuum, in liquid environment, and under spatial confinement by a solid overlayer are investigated in large-scale atomistic simulations. The simulations are performed in the regime of melting and resolidification, below the thresholds for laser spallation or ablation.

For single crystal (001) Ag targets with free surfaces, the formation of a nanocrystalline region with random crystallographic orientation of nanograins is only observed under irradiation conditions leading to the generation of sub-surface voids in the transiently melted surface region of the target. The presence of voids slows down the propagation of the epitaxial resolidification front and creates the conditions for reaching the critical level of undercooling required for the onset of a massive homogeneous nanocrystallization. The generation of sub-surface voids can be avoided by reducing the laser fluence or increasing the laser pulse duration. When no voids are generated, however, the resolidification proceeds through the solidification front propagation from the bulk of the target, and the maximum undercooling of the melted surface is not sufficient for the activation of homogeneous surface nanocrystallization. Due to the rough morphology of the liquid-solid interface created by the rapid laser-induced melting, the resolidification in this case produces surface microstructure featuring grains that are slightly misoriented with respect to each other and are separated by low angle grain boundaries or dislocation walls.

The presence of a liquid or solid overlayer suppresses the generation of strong tensile stresses responsible for the formation of sub-surface voids, provides an additional pathway for cooling through the heat conduction to the overlayer, and facilitates the formation of nanocrystalline structure in a region of the metal target adjacent to the overlayer. The higher acoustic impedance of the solid silica overlayer makes it more efficient, as compared to the water environment, in reducing the tensile stresses and extending the range of fluences that do not produce sub-surface voids or spallation. It is also found that the stabilizing effect of the solid overlayer may result in an incomplete melting of metal in the vicinity of the overlayer. In this case, the growth of the surviving crystallites from the metal-overlayer interface prevents the homogeneous nucleation of randomly-oriented crystallites and results in the formation of a nanocrystalline interfacial region with small grain misorientation. In all simulations, the nanocrystalline layers generated by laser processing of single-crystal Ag targets are characterized by a high density of stacking faults, twin boundaries, and point defects produced in the course of the rapid resolidification. The strong effect of the solid and liquid overlayers on laser-generated surface microstructure suggests a potential use of the overlayers in laser processing aimed at inducing surface nanocrystallization and achieving desired optical and mechanical properties of the surface.

The general conclusions derived in this study from the simulations of laser interactions with Ag targets are also applicable to other metals and alloys, although quantitative aspects may be sensitive to specific properties of target materials. In particular, while the presence of liquid or solid overlayers can be expected to facilitate the formation of nanocrystalline surface structure in short pulse laser processing of various systems, the conclusion that nanocrystallization is not possible for targets with free surfaces without the formation of sub-surface voids is specific to the (001) Ag target and may not hold for a different material system or even different crystallographic surface orientations of the same target.

Finally, we note that the nanocrystalline surface structures generated by short pulse melting and resolidification of one-component metal targets will have limited thermal stability and are likely to undergo grain coarsening beyond the timescale of simulations. In order to mitigate the grain coarsening and stabilize the nanocrystalline surface structures, the addition of appropriate alloying elements (solute) [53–55] during the laser synthesis can be a viable strategy from kinetic and thermodynamic perspectives. The solute atoms can preferably segregate to grain boundaries, thus reducing the free energy of nanocrystalline structures [56–58] and acting as obstacles for grain boundary migration [59,60].

Acknowledgments

Financial support for this work was provided by the National Science Foundation (NSF) through Grants CMMI-1301298 and CMMI-1436775. Computational support was provided by the Oak Ridge Leadership Computing Facility (INCITE project MAT130) and NSF through the Extreme Science and Engineering Discovery Environment (project TG-DMR110090). L.V.Z. also acknowledges support from the Austrian Science Fund (FWF) through the Lise Meitner Programme (project M 1984). C.-Y.S. acknowledges visiting researcher support from the Center for Nanointegration Duisburg-Essen (CENIDE), University of Duisburg-Essen, Germany.

Appendix A. Supplementary data

Supplementary data associated with this article can be found, in the online version, at http://dx.doi.org/10.1016/j.apsusc.2017.02.030.

References

[1] V. Amendola, M. Meneghetti, What controls the composition and the structure of nanomaterials generated by laser ablation in liquid solution? Phys. Chem. Chem. Phys. 15 (2013) 3027–3046.

[2] S. Ibrahimkutty, P. Wagener, T. dos Santos Rolo, D. Karpov, A. Menzel, T. Baumbach, S. Barcikowski, A. Plech, A hierarchical view on material formation during pulsed-laser synthesis of nanoparticles in liquid, Sci. Rep. 5 (2015) 16313.
[3] S. Reich, P. Schönfeld, P. Wagener, A. Letzel, S. Ibrahimkutty, B. Gökce, S. Barcikowski, A. Menzel, T. dos Santos Rolo, A. Plech, Pulsed laser ablation in liquids: impact of the bubble dynamics on particle formation, J. Colloid Interface Sci. 489 (2017) 106–113.
[4] M.E. Povarnitsyn, T.E. Itina, Hydrodynamic modeling of femtosecond laser ablation of metals in vacuum and in liquid, Appl. Phys. A 117 (2014) 175–178.
[5] C.-Y. Shih, C. Wu, M.V. Shugaev, L.V. Zhigilei, Atomistic modeling of nanoparticle generation in short pulse laser ablation of thin metal films in water, J. Colloid Interface Sci. 489 (2017) 3–17.
[6] W.T. Nichols, T. Sasaki, N. Koshizaki, Laser ablation of a platinum target in water. I. Ablation mechanisms, J. Appl. Phys. 100 (2006) 114911.
[7] E.V. Zavedeev, A.V. Petrovskaya, A.V. Simakin, G.A. Shafeev, Formation of nanostructures upon laser ablation of silver in liquids, Quantum Electron. 36 (2006) 978–980.
[8] E. Stratakis, V. Zorba, M. Barberoglou, C. Fotakis, G.A. Shafeev, Laser writing of nanostructures on bulk Al via its ablation in liquids, Nanotechnology 20 (2009) 105303.
[9] G.K. Podagatlapalli, S. Hamad, S. Sreedhar, S.P. Tewari, S.V. Rao, Fabrication and characterization of aluminum nanostructures and nanoparticles obtained using femtosecond ablation technique, Chem. Phys. Lett. 530 (2012) 93–97.
[10] S.V. Rao, G.K. Podagatlapalli, S. Hamad, Ultrafast laser ablation in liquids for nanomaterials and applications, J. Nanosci. Nanotechnol. 14 (2014) 1364–1388.
[11] S. Bashir, M.S. Rafique, C.S. Nathala, W. Husinsky, The formation of nanodimensional structures on the surface of tin exposed to femtosecond laser pulses in the ambient environment of ethanol, Appl. Surf. Sci. 290 (2014) 53–58.
[12] R. Kuladeep, M.H. Dar, K.L.N. Deepak, D.N. Rao, Ultrafast laser induced periodic sub-wavelength aluminum surface structures and nanoparticles in air and liquids, J. Appl. Phys. 116 (2014) 113107.
[13] E.V. Barmina, G.A. Shafeev, P.G. Kuzmin, A.A. Serkov, A.V. Simakin, N.N. Melnik, Laser-assisted generation of gold nanoparticles and nanostructures in liquid and their plasmonic luminescence, Appl. Phys. A 115 (2014) 747–752.
[14] A.A. Serkov, E.V. Barmina, G.A. Shafeev, V.V. Voronov, Laser ablation of titanium in liquid in external electric field, Appl. Surf. Sci. 348 (2015) 16–21.
[15] J.-H. Klein-Wiele, P. Simon, Sub-100 nm pattern generation by laser direct writing using a confinement layer, Opt. Express 21 (2013) 9017–9023.
[16] J. Ihlemann, R. Weichenhain-Schriever, Pulsed laser-induced formation of silica nanogrids, Nanoscale Res. Lett. 9 (2014) 102.
[17] E.T. Karim, M.V. Shugaev, C. Wu, Z. Lin, H. Matsumoto, M. Conneran, J. Kleinert, R.F. Hainsey, L.V. Zhigilei, Experimental characterization and atomistic modeling of interfacial void formation and detachment in short pulse laser processing of metal surfaces covered by solid transparent overlayers, Appl. Phys. A 122 (2016) 407.
[18] B.P. Fairand, B.A. Wilcox, W.J. Gallagher, D.N. Williams, Laser shock-induced microstructural and mechanical property changes in 7075 aluminum, J. Appl. Phys. 43 (1972) 3893–3895.
[19] R. Fabbro, J. Fournier, P. Ballard, D. Devaux, J. Virmont, Physical study of laser-produced plasma in confined geometry, J. Appl. Phys. 68 (1990) 775–784.
[20] X. Wu, Z. Duan, H. Song, Y. Wei, X. Wang, C. Huang, Shock pressure induced by glass-confined laser shock peening: experiments, modeling and simulation, J. Appl. Phys. 110 (2011) 053112.
[21] X. Sedao, M.V. Shugaev, C. Wu, T. Douillard, C. Esnouf, C. Maurice, S. Reynaud, F. Pigeon, F. Garrelie, L.V. Zhigilei, J.-P. Colombier, Growth twinning and generation of high-frequency surface nanostructures in ultrafast laser-induced transient melting and resolidification, ACS Nano 10 (2016) 6995–7007.
[22] C. Wu, M.S. Christensen, J.-M. Savolainen, P. Balling, L.V. Zhigilei, Generation of subsurface voids and a nanocrystalline surface layer in femtosecond laser irradiation of a single-crystal Ag target, Phys. Rev. B 91 (2015) 035413.
[23] R.Z. Valiev, I.V. Alexandrov, Y.T. Zhu, T.C. Lowe, Paradox of strength and ductility in metals processed by severe plastic deformation, J. Mater. Res. 17 (2002) 5–8.
[24] M.A. Meyers, A. Mishra, D.J. Benson, Mechanical properties of nanocrystalline materials, Prog. Mater. Sci. 51 (2006) 427–556.
[25] T.H. Fang, W.L. Li, N.R. Tao, K. Lu, Revealing extraordinary intrinsic tensile plasticity in gradient nano-grained copper, Science 331 (2011) 1587–1590.
[26] X. Li, M. Dao, C. Eberl, A.M. Hodge, H. Gao, Fracture, fatigue, and creep of nanotwinned metals, MRS Bull. 41 (2016) 298–304.
[27] M.L. Trudeau, J.Y. Ying, Nanocrystalline materials in catalysis and electrocatalysis: Structure tailoring and surface reactivity, Nanostruct. Mater. 7 (1996) 245–258.
[28] J.K. Nørskov, T. Bligaard, B. Hvolbæk, F. Abild-Pedersen, I. Chorkendorff, C.H. Christensen, The nature of the active site in heterogeneous metal catalysis, Chem. Soc. Rev. 37 (2008) 2163–2171.
[29] Y. Lu, H. Zhang, F. Liu, UV–visible reflectance spectra of nanocrystalline silver compacted under different pressures, Phys. Lett. A 342 (2005) 351–356.
[30] D.S. Ivanov, L.V. Zhigilei, Combined atomistic-continuum modeling of short-pulse laser melting and disintegration of metal films, Phys. Rev. B 68 (2003) 064114.
[31] M.P. Allen, D.J. Tildesley, Computer Simulation of Liquids, Clarendon Press, Oxford, 1987.
[32] S.I. Anisimov, B.L. Kapeliovich, T.L. Perel'man, Electron emission from metal surfaces exposed to ultrashort laser pulses, Sov. Phys. JETP 39 (1974) 375–377.
[33] S.-S. Wellershoff, J. Hohlfeld, J. Güdde, E. Matthias, The role of electron-phonon coupling in femtosecond laser damage of metals, Appl. Phys. A 69 (1999) S99–S107.
[34] D. Bäuerle, Laser Processing and Chemistry, Springer-Verlag, Berlin, Heidelberg, 2000.
[35] E.T. Karim, M. Shugaev, C. Wu, Z. Lin, R.F. Hainsey, L.V. Zhigilei, Atomistic simulation study of short pulse laser interactions with a metal target under conditions of spatial confinement by a transparent overlayer, J. Appl. Phys. 115 (2014) 183501.
[36] L.V. Zhigilei, B.J. Garrison, Pressure waves in microscopic simulations of laser ablation, Mat. Res. Soc. Symp. Proc. 538 (1999) 491–496.
[37] C. Schäfer, H.M. Urbassek, L.V. Zhigilei, B.J. Garrison, Pressure-transmitting boundary conditions for molecular-dynamics simulations, Comput. Mater. Sci. 24 (2002) 421–429.
[38] S.M. Foiles, M.I. Baskes, M.S. Daw, Embedded-atom-method functions for the fcc metals Cu, Ag Au, Ni, Pd, Pt, and their alloys, Phys. Rev. B 33 (1986) 7983–7991.
[39] M. Tabetah, A. Matei, C. Constantinescu, N.P. Mortensen, M. Dinescu, J. Schou, L.V. Zhigilei, The minimum amount of matrix needed for matrix-assisted pulsed laser deposition of biomolecules, J. Phys. Chem. B 118 (2014) 13290–13299.
[40] J. Zou, C. Wu, W.D. Robertson, L.V. Zhigilei, R.J.D. Miller, Molecular dynamics investigation of desorption and ion separation following picosecond infrared laser (PIRL) ablation of an ionic aqueous protein solution, J. Chem. Phys. 145 (2016) 204202.
[41] L.V. Zhigilei, B.J. Garrison, Microscopic mechanisms of laser ablation of organic solids in the thermal and stress confinement irradiation regimes, J. Appl. Phys. 88 (2000) 1281–1298.
[42] E. Leveugle, D.S. Ivanov, L.V. Zhigilei, Photomechanical spallation of molecular and metal targets: molecular dynamics study, Appl. Phys. A 79 (2004) 1643–1655.
[43] G. Paltauf, P.E. Dyer, Photomechanical processes and effects in ablation, Chem. Rev. 103 (2003) 487–518.
[44] L.V. Zhigilei, Z. Lin, D.S. Ivanov, Atomistic modeling of short pulse laser ablation of metals: connections between melting, spallation, and phase explosion, J. Phys. Chem. C 113 (2009) 11892–11906.
[45] C. Wu, L.V. Zhigilei, Nanocrystalline and polyicosahedral structure of a nanospike generated on metal surface irradiated by a single femtosecond laser pulse, J. Phys. Chem. C 120 (2016) 4438–4447.
[46] C. Deng, F. Sansoz, Fundamental differences in the plasticity of periodically twinned nanowires in Au, Ag, Al, Cu, Pb and Ni, Acta Mater. 57 (2009) 6090–6101.
[47] http://www.faculty.virginia.edu/CompMat/laser-surface-nanostructuring/.
[48] C. Wu, D.A. Thomas, Z. Lin, L.V. Zhigilei, Runaway lattice-mismatched interface in an atomistic simulation of femtosecond laser irradiation of Ag film–Cu substrate system, Appl. Phys. A 104 (2011) 781–792.
[49] D.S. Ivanov, L.V. Zhigilei, Effect of pressure relaxation on the mechanisms of short-pulse laser melting, Phys. Rev. Lett. 91 (2003) 105701.
[50] Z. Lin, L.V. Zhigilei, V. Celli, Electron-phonon coupling and electron heat capacity of metals under conditions of strong electron-phonon nonequilibrium, Phys. Rev. B 77 (2008) 075133.
[51] D.S. Ivanov, L.V. Zhigilei, Kinetic limit of heterogeneous melting in metals, Phys. Rev. Lett. 98 (2007) 195701.
[52] W.-L. Chan, R.S. Averback, D.G. Cahill, Y. Ashkenazy, Solidification velocities in deeply undercooled silver, Phys. Rev. Lett. 102 (2009) 095701.
[53] C.C. Koch, R.O. Scattergood, K.A. Darling, J.E. Semones, Stabilization of nanocrystalline grain sizes by solute additions, J. Mater. Sci. 43 (2008) 7264–7272.
[54] F. Liu, R. Kirchheim, Comparsion between kinetic and thermodynamic effects on grain growth, Thin Solid Films 466 (2004) 108–113.
[55] A.J. Darling, Y. Roberts, S.N. Mishin, Grain size stabilization of nanocrystalline copper at high temperature by alloying with tantalum, J. Alloys Compd. 573 (2013) 142–150.
[56] M. Saber, H. Kotan, C.C. Koch, R.O. Scattergood, Thermodynamic stabilization of nanocrystalline binary alloys, J. Appl. Phys. 113 (2013) 063515.
[57] K.A. Darling, M.A. Tschopp, B.K. VanLeeuwen, M.A. Atwater, Z.K. Liu, Mitigating grain growth in binary nanocrystalline alloys through solute selection based on thermodynamic stability maps, Comput. Mater. Sci. 84 (2014) 255–266.
[58] T. Chookajorn, H.A. Murdoch, C.A. Schuh, Design of stable nanocrystalline alloys, Science 337 (2012) 951–954.
[59] K. Lücke, K. Detert, A quantitative theory of grain-boundary motion and recrystallization in metals in the presence of impurities, Acta Metall. 5 (1957) 628–637.
[60] M. Hillert, B. Sundman, A treatment of the solute drag on moving grain boundaries and phase interfaces in binary alloys, Acta Metall. 24 (1976) 731–743.